Gold-Like Activity, Copper-Like Selectivity of Heteroatomic Transition Metal Carbides (M2C) for Electrocatalytic Carbon Dioxide Reduction Reaction

Mohammadreza Esmaeilirad
Illinois Institute of Technology https://orcid.org/0000-0002-1575-2892
Artem Baskin
Lawrence Berkeley National Laboratory https://orcid.org/0000-0002-3156-6256
Alireza Kondori
Illinois Institute of Technology https://orcid.org/0000-0001-6959-2292
Ana Sanz Matias
Lawrence Berkeley National Laboratory https://orcid.org/0000-0002-4662-5140
Jin Qian
Lawrence Berkeley National Laboratory
Boao Song
University of Illinois at Chicago https://orcid.org/0000-0003-3124-3235
Mahmoud Tamadoni Saray
University of Illinois at Chicago
Kamil Kucuk
Illinois Institute of Technology https://orcid.org/0000-0002-7356-9754
Andres Ruiz Belmonte
Illinois Institute of Technology
Pablo Navarro Munoz Delgado
Illinois Institute of Technology
Junwon Park
Illinois Institute of Technology
Rahman Azari
Pennsylvania State University
Carlo Segre
Illinois Institute of Technology https://orcid.org/0000-0001-7664-1574
Reza Shahbazian-Yassar
University of Illinois at Chicago https://orcid.org/0000-0002-7744-4780
David Prendergast
Lawrence Berkeley National Laboratory https://orcid.org/0000-0003-0598-1453
Mohammad Asadi (masadi1@iit.edu)

Illinois Institute of Technology https://orcid.org/0000-0003-0354-2473

Article

Keywords: electrochemical carbon dioxide reduction reaction, two-dimensional transition metal carbide , Heteroatomic Transition Metal Carbides

Posted Date: March 23rd, 2021

DOI: https://doi.org/10.21203/rs.3.rs-244769/v1

Abstract

An overarching challenge of the electrochemical carbon dioxide reduction reaction (eCO_2RR) is finding an earth-abundant, highly active catalyst that selectively produces hydrocarbons at relatively low overpotentials. Here, we have studied the two-dimensional transition metal carbide (TMC) class of materials and found that di-tungsten carbide (W_2C) nanoflakes exhibit maximum methane (CH_4) current density of -421.63 mA/cm^2 and a CH_4 faradic efficiency of 82.7%±2% in a hybrid electrolyte of 3 M potassium hydroxide (KOH) and 2 M choline-chloride (CC). Powered by a triple junction photovoltaic cell, we have demonstrated a flow electrolyzer that uses humidified CO_2 to produce CH_4 in a 700-hours process under one sun illumination with a CO_2RR energy efficiency of about 62.3% and a solar-to-fuel efficiency of 20.7%. Density functional theory (DFT) calculations reveal that dissociation of water, chemisorption of CO_2 and cleavage of the C-O bond – the most energy consuming elementary steps in other catalysts such as copper – become nearly spontaneous at the W_2C surface. This results in instantaneous formation of adsorbed CO – an important reaction intermediate – and an unlimited source of protons near the tungsten surface sites that are the main reasons for the observed superior activity, selectivity, and small potential.

Main Text

The electrocatalytic carbon dioxide reduction reaction (eCO_2RR) driven by renewable energy has great potential for the sustainable production of chemicals and fuels at the gigaton scale that can be used any time, any place[1–4]. It also offers a promising way to store energy in chemical bonds due to having nearly two orders of magnitude higher energy density compared to the most advanced battery technologies[5]. However, reducing CO_2 to value-added chemicals is both costly and slow based on intrinsic thermodynamics and kinetics, making the goal of an effective and feasible process a real challenge[6–9].

Conventional pure metal catalysts such as gold (Au), palladium (Pd), silver (Ag) and newly developed transition metal dichalcogenides (TMDCs)[8,10–18] are known to exhibit high activities for the CO_2RR in different electrolyte solutions[19–26]. However, these catalysts are mainly selective for carbon monoxide (CO), known as an intermediate product[8,27]. Other catalysts such as copper (Cu) and Cu-based catalysts have the ability to reduce CO_2 to various chemicals such as methane (CH_4), ethylene (C_2H_4), formic acid (HCOOH), methanol (CH_3OH), and ethanol (C_2H_5OH)[28–36]. Despite their good selectivity, these catalysts require high potentials –excess energy– to achieve suitable current densities –reaction rates– impeding their use for effective production of chemicals and fuels[37,38]. Therefore, a novel catalyst with outstanding electronic properties needs to be developed to selectively produce hydrocarbons at high rates at relatively low potentials.

Heteroatomic transition metal carbide (TMC) catalysts, also known as MXenes, have recently received great attention for various electrocatalytic reactions due to their unique structural and electronic properties[39–42]. In particular, M_2C (M denotes transition metals) stoichiometry of this class of two-dimensional materials forms layered structures of M-C-M where a plane of carbon atoms is sandwiched between two hexagonal planes of metal atoms. This structure provides a high density of active metal atoms at the surface breaking conventional scaling relationships that limit electrocatalytic performance of their counterparts such as TMDCs and pure metals[43]. However, there is limited knowledge of their performance and characteristics as eCO_2RR catalysts under actual experimental conditions.

Here, we have studied the performance of di-tungsten carbide (W_2C), di-molybdenum carbide (Mo_2C) di-niobium carbide (Nb_2C) and di-vanadium carbide (V_2C) nanoflakes (NFs) as inexpensive, non-precious members of TMCs for eCO_2RR.

The TMC NFs i.e., W_2C, Mo_2C, Nb_2C and V_2C were synthesized using a carburization process followed by the liquid exfoliation technique (Supplementary section S1)[27,44,45]. The electrocatalytic performance of TMC NFs with the similar crystallite sizes (25.4±5 nm) were then studied in a three-electrode cell and compared with Au and Cu nanoparticles (NPs), conventional catalysts for this reaction,[46] under identical experimental conditions (Supplementary section S2). To improve the CO_2RR performance in competing with hydrogen evolution reaction (HER), we have employed a mixture of 3 M potassium hydroxide (KOH) and 2 M choline-chloride (CC) solution (KOH:CC (3M:2M)) as the electrolyte in this study[47].

The linear sweep voltammetry (LSV) experiments and a real time product stream analysis show that CO_2RR on the W_2C surface starts at a potential of -122.7 mV vs reversible hydrogen electrode (RHE) by producing CO and H_2 and reach maximum CO_2RR current density (j_{CO2RR}) of -548.9 mA/cm^2 at -1.05 V vs RHE (Supplementary Figs. S2-4 and Fig. 1a). As shown in Fig. 1a, j_{CO2RR} of -419.9, -381.9 and -350.8 mA/cm^2 were observed for Mo_2C, Nb_2C, and V_2C NFs, respectively, at this potential (Supplementary section S3). However, Au and Cu NPs exhibit a j_{CO2RR} of -208.11 and -89.53 mA/cm^2 at -1.05 V vs RHE (Fig. 1a). The selectivity analysis also indicates that TMC NFs produce hydrocarbons (i.e., CH_4, C_2H_4, CH_3OH and C_2H_5OH) at a potential range of -0.45 to -1.05 V vs RHE for W_2C, Mo_2C and Nb_2C NFs and a potential range of -0.55 to -1.05 V vs RHE for V_2C NFs where CH_4 is identified as the main product (Supplementary section S3).

Figure 1b illustrates CH_4 formation current densities (j_{CH4}, mA/cm^2) of the TMC NFs compared to Cu NPs, a conventional catalyst for hydrocarbon production. The partial current densities of different products (*i.e.*, H_2, CO, CH_4, C_2H_4, CH_3OH and C_2H_5OH) were calculated by multiplying FEs and total current densities at different potentials (Supplementary section S3 and Fig. S3). As shown in Fig. 1b, a maximum j_{CH4} of -421.63 mA/cm^2 is obtained for W_2C NFs at a potential of -1.05 V vs RHE where Nb_2C NFs, Mo_2C NFs, and V_2C NFs show values of -219.16, -211.33, and -147.56 mA/cm^2, respectively, at this potential. We also compared the CH_4 formation activity of TMCs *i.e.*, W_2C, Nb_2C, Mo_2C, and V_2C NFs with

state-of-the-art catalysts in the literature (Supplementary Table S2)[46,48–54]. Supplementary Table S2b indicates that the j_{CH4} of W_2C NFs is 3.6 and 4.2 times higher than recently studied La_2CuO_4 (-117 mA/cm^2 at -1.4 V vs RHE)[51] and Cu-N (-100 mA/cm^2 at -1.0 V vs RHE)[48], respectively. The partial current densities of other hydrocarbon products i.e., C_2H_4, CH_3OH and C_2H_5OH are also shown in Fig. S3 (Supplementary section S3).

To evaluate the intrinsic activity of W_2C NFs, we measured CH_4 formation turnover frequency (TOF_{CH4}) by normalizing its activity to the number of active atoms at the surface using roughness factor method and compared it with the other catalysts in this study (Supplementary section S5). Our calculations indicate a TOF_{CH4} of 10.42 s^{-1} at a potential of -1.05 V vs RHE for W_2C NFs; by comparison, TOF_{CH4} of 4.54, 3.74 and 2.79 s^{-1} were calculated for Mo_2C NFs, Nb_2C NFs, and V_2C NFs, respectively. The calculated TOF_{CH4} of W_2C NFs at the potential of -1.05 V vs RHE is about 2 orders of magnitude higher than that of Cu NPs (0.0736 s^{-1}) under identical experimental conditions (Supplementary Fig. S7a). Moreover, total CO_2RR turnover frequencies (TOF_{CO2RR}) of 19.09, 19.36, 17.82, 17.55 s^{-1} were calculated for W_2C NFs, Mo_2C NFs, Nb_2C NFs, and V_2C NFs, respectively, where Au NPs and Cu NPs exhibit TOF_{CO2RR} of 4.35 and 0.1956 s^{-1}, respectively (Supplementary Fig. S7f). These results suggest the superior CH_4 selectivity of TMC catalysts compared to state-of-the-art catalysts[48–51,54–57].

Furthermore, we performed a comparative mechanistic study by calculating Tafel slopes for different products to gain insight about the eCO_2RR mechanism of the TMCs *i.e.*, W_2C, Mo_2C, Nb_2C, and V_2C NFs in the two-compartment three-electrode electrochemical cell (Supplementary section S6, Fig. S8) [58]. Our Tafel plot analyses show that the TMC NFs possess steeper Tafel slopes, and therefore a weaker potential dependence compared with Cu NPs for the formed products (*i.e.*, CO, CH_4 and C_2H_4) (Supplementary Fig. S8)[58]. The Tafel plot analyses suggest a different CO_2RR mechanism for TMC NFs than that of Cu catalysts where C-O bond scission is the rate determining step[58].

To gain more insight to the remarkable performance of these catalysts for electrocatalytic CO_2RR, the structural and physicochemical properties of TMC NFs were characterized at molecular and atomic scales by performing X-ray diffraction (XRD), X-ray photoelectron spectroscopy (XPS), and scanning transmission electron microscopy (STEM) (Supplementary sections S7-9). At first, we have performed XPS experiments to analyze the surface chemistry of TMC NFs. XPS analysis (Supplementary Fig. S9) indicates that our NF samples contain metallic TMCs, with little or no evident surface oxidation. The results show that the chemical composition of the surface, the empirical formula of M_2C (M: transition metal, C: Carbide) and the oxidation state of +2 for the transition metals *i.e.*, W, Mo, Nb, and V are similar in all synthesized TMCs (Supplementary section S7). The lattice structure and crystallite size of the TMC NFs were then studied by performing XRD experiments. The XRD pattern of W_2C NFs shows a sharp peak at 39.91º along with three pronounced peaks at 34.84º, 38.54º, and 52.65º corresponding to (101), (100), (002) and (102) crystal surfaces of W_2C, respectively. The XRD spectra of the TMCs show all Bragg peaks

of W_2C, Mo_2C, Nb_2C, and V_2C NFs; verifying their homogenous and pure structures. The XRD results indicate a constant dominant lattice plane of (101) and a similar average crystallite size of 25.4±5 nm for all synthesized TMCs (Supplementary Fig. S10) [59–61].

Furthermore, we performed atomic scale STEM experiments to study surface atom coordination, crystallite sizes and dominant plane structures of TMC NFs (Supplementary Fig. S11-18). Figures 2a-d show STEM results of W_2C NFs. Figures 2a and b indicate high-angle annular dark-field (HAADF) image and corresponding fast Fourier transforms (FFT) of W_2C NFs in the <101> zone axis. The atomic models of the <101> zone axis and bright field (BF) image of W_2C NFs are represented in Figs. 2c and d, respectively. Figure 2d indicates the carbon atomic columns in the red box and the intensity profile across the red box region showing that the distance between two carbon atoms is 2.55 Å. The STEM results of other TMCs *i.e.*, Mo_2C, Nb_2C, and V_2C NFs are explained in Supplementary section S9. The STEM and XRD results of synthesized TMC NFs confirm that the structure of these materials is a perfect match with standard 1T structure, suggesting a tetragonal symmetry and octahedral coordination of the atoms (Fig. 2e) [43,62]. Figure 2e indicates the schematic of 1T structure TMC NFs showing tetragonal symmetry, one layer per repeat unit with octahedral coordination. The lattice constant *a* is in the range of 3.07 to 3.15 Å for synthesized TMC NFs. The stacking index *b* indicates the interlayer spacing which is in the range of 4.53 to 5 Å for studied TMCs. As shown in Fig. 2e, 1T atomic coordination provides metal-terminated surface atoms that are known to be favorable binding sites of adsorbed intermediates in eCO_2RR [43,62]. Our atomic and molecular scale structural analyses indicate that the synthesized TMC NFs have fairly similar structural properties *e.g.*, (1T) crystalline structure with a dominant plane of (101), crystallite sizes, and atomic coordination.

To further discern the difference between the observed electrocatalytic performance of the TMCs, we have studied their electronic properties by performing electrochemical impedance spectroscopy (EIS) (Supplementary section S10) and, work function measurements using ultraviolet photoelectron spectroscopy (UPS) (Supplementary section S11)[8]. At first, we have employed the EIS experiments to compare the overall electron-transfer properties of the TMC catalysts in the double layer region (Supplementary section S10). To do this, TMC NFs with similar structural and physical properties e.g., sizes, shapes, and mass loadings (0.1 mg/cm^2) coated on glass carbon were used as the working electrodes. This results in similar roughness, morphology, intrinsic capacitance, and exposed surface area of the studied samples confirmed by our characterization results (Supplementary sections S5-9). The EIS experiments have been performed at a potential of -310 mV vs RHE for all TMCs under identical experimental conditions (Supplementary section S10). Figure 2f shows the fitted EIS spectra of each TMC catalyst using Randles circuit model, indicating a smaller charge transfer resistance (R_{ct}) for W_2C NFs (~17 ohms) compared to the other TMCs, *i.e.*, Mo_2C NFs (~25 ohm), Nb_2C NFs (~33 ohm), and V_2C NFs (~38 ohm)[63]. The UPS method also was used to compare the surface work function of TMCs (Fig. 2g). The results indicate a lower work function for W_2C NFs (0.2 to 0.84 eV) compared to Mo_2C NFs (3.92 eV), Nb_2C NFs (4.44 eV), and V_2C NFs (4.55 eV). The charge transfer resistance obtained by EIS

experiments and the surface work function value measured by UPS experiments suggest the superior activity of W_2C NFs compared to other TMCs in this study *i.e.*, Mo_2C, Nb_2C, and V_2C NFs.

In addition to our experimental observations, we have performed density functional theory (DFT) calculations to gain more insight to the electronic and catalytic properties of M_2C compounds. The aim is to address the enhanced activity and selectivity of these TMCs and to explore both electrochemical (*i.e.*, driven) and chemical (*i.e.*, favorable or spontaneous) processes that distinguish them from other catalysts, such as Au and Cu.

With respect to activity, the electronic density of states (DOS) indicate that transition metal *d* states dominate at the Fermi level of these TMCs, much more so than elemental Au, another high activity catalyst. Bader charge calculations indicate that metal atoms at TMC surface are significantly more reduced compared to the bulk atoms (Fig. 2h, Supplementary Fig. S24). These results indicate the increased availability of electrons at metal-rich TMC surfaces, which may increase the catalytic activity of TMC NFs.

With respect to the increased selectivity of TMC NFs, especially for CH_4 production, we have explored the CO_2RR pathway on the W_2C (101) surface in detail by using DFT calculations. Focusing initially on electrochemical processes, we employed the computational hydrogen electrode (CHE) model[64–66] (Supplementary Tables S7 and S8) to explore the stepwise electronic reduction and protonation of adsorbed species in the low molecular coverage limit. The lowest free energy pathway to produce CH_4 with only electrochemical steps is shown in Fig. 3 (see a more detailed path in Supplementary Fig. S25), indicating limiting steps (at zero potential with respect to RHE) that involve protonation of adsorbed CO_2 and O, and, most importantly, the desorption of H_2O following protonation of adsorbed OH. The difficulty of this final step is not surprising, as W_2C (101) strongly adsorbs and spontaneously dissociates water (,) without electrochemical assistance. Similarly, our calculations indicate that W_2C (101) strongly chemisorbs CO_2 (, bond length) in contrast to normally weak physisorption on Cu ( ) and other catalyst surfaces[28,67–69]. Furthermore, the (101) surface of W_2C enables favorable and unassisted dissociation of adsorbed CO_2 (, , Supplementary Table S9) suggesting that C–O bond scission may take place in the early stages of CO_2 reduction, skipping the uphill production of adsorbed carboxyl. Based on these findings, we propose that W_2C (101) distinguishes itself as a catalyst due to an interplay between surface-assisted chemical steps, whose energetics will depend on the local chemical equilibrium at the surface and electrochemical steps that reduce pre-existing surface reagents and open up new pathways for the overall reaction to proceed. More detailed studies of such cooperative catalytic processes and their limiting steps may be encouraged based on the promise of W_2C as a high-performance CO_2 reduction catalyst. Here, we highlight the plausible cooperative effects of these steps, which set apart W_2C from conventional noble metal catalysts and the other TMCs, specially for CH_4 production. The immediate benefit of the favorable chemical processes mentioned above should be a higher surface coverage of CO_2 (and consequently CO) and an excess of surface protons. This may explain the high

Faradaic efficiencies for production of both H_2 and CO at low potentials (see Supplementary section S3 and Table S1). However, once a limiting potential (-0.74 V estimate) is reached, the readily protonated products of adsorbed CO that produce CH_4 are no longer hindered by a build-up of adsorbed byproducts (O* then OH*), which can now be protonated and released from the surface.

We can divide the complex, multistep reaction into two key parts: initial conversion of adsorbed CO_2 to adsorbed CO, followed by conversion of adsorbed CO to CH_4 with the release of H_2O (see Fig. 3). As indicated in Fig. 3, the first part, generation of adsorbed CO, can be achieved by chemical or electrochemical means. We have direct and favorable chemical conversion of adsorbed CO_2 to adsorbed CO and O on W_2C (101), but also two electrochemical pathways: production of HO-CO* in a single step (+0.66 eV, Fig. 3) or an alternative initially favorable protonation to OCHO* followed by two uphill electrochemical steps producing first OCH_2O* followed by release of H_2 and the final product of HO-CO* with a similar free energy cost (+0.68 eV, Supplementary Fig. S25 and Table S9). A final electrochemically driven protonation of HO-CO* favorably releases H_2O and leaves CO*.

With chemically or electrochemically generated adsorbed CO, we can proceed to the second part of the overall reaction to produce CH_4 from CO_2, which involves multiple favorable protonation steps. The W_2C catalyst distinguishes itself here. The electrochemical activation of remains thermodynamically favorable (ΔG = -0.26 eV) on W_2C (101), whereas on other catalysts, such as Cu, this process is usually uphill with the potential ranging from -0.74 V to -0.97 V vs RHE[66,70]. Moreover, due to the spontaneous water dissociation, the direct H* transfer step on W_2C could be even more favorable with a resultant ΔG= -0.433 eV (Supplementary Table S9). The next two electrochemical steps are downhill (ΔG = -0.04 and -0.58 eV): the first forming the unstable methoxy radical with oxygen attached to a surface W atom; the second leading to spontaneous dissociation into the methyl radical and a surface oxygen atom . The electrochemical conversion of the surface into CH_4 is favorable (ΔG = -0.43 eV) and the protonation of the surface oxygen is only slightly uphill (ΔG = +0.03 eV). As we already stated, for the overall reaction on W_2C (101) it is the final protonation of to release H_2O that is the limiting step (ΔG = +0.74 eV).

We also compared W_2C with the other TMCs studied by calculating the energies of adsorption of water and CO_2 as well as the potentials of the rate determining step (*i.e.*, protonation of) for Nb_2C, Mo_2C, and V_2C (Supplementary Table S10). Our calculations indicate that these TMCs also strongly chemisorb CO_2 with adsorption energies of -1.32, -1.62, and -0.96 eV, respectively. Moreover, Nb_2C also shows favorable C–O bond scission of adsorbed CO_2. Additionally, Nb_2C, Mo_2C, and V_2C strongly adsorb water with the energies of -1.87, -1.23 and -0.59 eV, respectively, where Nb_2C is the only other catalyst that dissociates water. In contrast to W_2C, the energies required for the protonation of are higher: +1.17, +1.25, +0.85 eV for Nb_2C, Mo_2C, and V_2C, respectively (Supplementary Table S10). Therefore, we can conclude that, within this set of four TMCs, W_2C possesses the optimal characteristics for efficient completion of CO_2RR: (1) sufficiently strong adsorption of CO_2, (2) spontaneous dissociation of water,

and (3) the lowest limiting potential for OH* protonation. We conclude that the performance of Nb_2C is reduced due to its stronger water adsorption, resulting in the protonation of requiring more energy. We would expect Mo_2C to have a lower surface coverage of protons and higher costs for the protonation of . The weakest CO_2 adsorption on V_2C decreases its surface coverage, making it the worst TMC catalyst here, despite its relatively small limiting reaction potential of protonation of OH*.

As we mentioned before, for W_2C the realistic network of pathways towards CH_4 consists of a potential dependent combination of competing chemical and electrochemical steps with the actual limiting potential being in the range from -0.483 V to -0.744 V vs RHE (see full path. Supplementary Fig. S25), which is consistent with our three-electrode electrochemical experimental results (Supplementary section S3 and Table S1). A steeper Tafel slope for CH_4 formation on W_2C than other TMCs and Cu, (Supplementary Fig. S8) also indicates the competition between reactions for the active sites on the catalyst surface. Specifically, the spontaneous water dissociation on W_2C (101) explains the ease of the HER in our non-acidic electrolyte where the source of protons is normally water. A weak potential dependence of the partial CO current and its small overpotential also originate from the interplay between chemical and electrochemical steps (see Supplementary Material for details).

Experimentally, we have studied the effect of choline chloride (CC) on the activity and selectivity of the TMC catalysts. To do this, we have performed electrochemical CO_2RR in different choline chloride concentrations of *i.e.*, 0.01, 0.1, 1, and 2 M mixed with 3 M KOH (Supplementary section S13). Figure 4 shows CO_2RR overall current density and different products (*i.e.*, CH_4, C_2H_4, CO, alcohols-CH_3OH and C_2H_5OH- and H_2) partial current densities for W_2C NFs in different CC concentration electrolytes. Figure 4a indicates that by increasing the concentration of CC in the electrolyte the CO_2RR current density (j_{CO2RR}) increases and reaches a maximum value of -548.89 mA/cm^2 at a potential of -1.05 V vs RHE for 2 M of CC. The obtained value is about 32, 24, 17, 9% higher than that of 0, 0.01, 0.1, and 1 M of CC, respectively. Moreover, a maximum CH_4 formation current density (j_{CH4}) of -421.63 mA/cm^2 is obtained for 2M CC at a potential of -1.05 V vs RHE that is about 1.41, 1.29, 1.19 and 1.1 times higher than that of 0, 0.01, 0.1, and 1 M, respectively (Fig. 4b).

The results also indicate using W_2C NFs, maximum partial current densities of other products i.e., C_2H_4 (j_{C2H4} of -35.84 mA/cm^2), CO (j_{CO} of -78.48 mA/cm^2), and alcohols ($j_{Alcohols}$ of -12.81 mA/cm^2; -6.84 mA/cm^2 for CH_3OH and -5.97 mA/cm^2 for C_2H_5OH) were obtained at the potential of -1.05 V vs RHE in 2M CC (Figs. 4b-d). In contrast, the measured H_2 partial current densities indicate that by adding higher concentration of CC to the electrolyte solution the rate of H_2 production decreases significantly where a minimum H_2 formation current density of -4.48 mA/cm^2 was obtained for 2 M CC at a potential of -0.85 V vs RHE that is 12.31, 8.97, 6.76, 3.23 times lower than that of 0, 0.01, 0.1 and 1 M CC, respectively.

These results suggest that adding choline chloride to the 3 M KOH electrolyte suppresses the competing hydrogen evolution reaction (HER) and increases the formation of CO_2RR products more specifically CH_4

[27].

The stability of the choline chloride electrolytes was studied by conducting nuclear magnetic resonance (NMR) and $^{13}CO_2$ isotope experiments (Supplementary section S14 and S15) [27,46,71]. The ^{1}H and ^{13}C NMR spectra reveal similar peak areas and chemical shifts for fresh and used electrolytes indicating no generation of new diamagnetic species or change in the choline chloride structure under applied potential of -1.05 V vs RHE (Supplementary Figs. S36 and S37). The $^{13}CO_2$ isotope experiments also show that the CO_2 gas present inside the electrolyte is the only source of the formed products in the electrochemical CO_2RR (Supplementary Fig. S39). These results confirm that choline chloride with different concentrations *i.e.*, 0, 01, 0.1, 1 and 2 M remains stable at the range of applied potentials in the electrochemical CO_2RR experiments.

Next, we studied the performance of W_2C NFs in our developed solid polymer electrolyte flow electrolyzer for continuous electrochemical CO_2RR using this catalyst as the cathode (Supplementary section S16). The flow electrolyzer used in this study consists of a two-compartment electrochemical setup with active area of 5 cm^2 coated with W_2C NFs at the cathode and iridium oxide nanoparticles (IrO_2 NPs) as the anode and were then fed with humidified CO_2 and KOH:CC (3M:2M) electrolyte, respectively (Supplementary section S16).

To study the CO_2RR performance of W_2C NFs in the flow electrolyzer, we performed chronoamperometry (CA) experiments at different cell potentials ranging from -1.5 to -2.3 V for W_2C NFs (Supplementary section S16). As shown in Fig. 5a, the results show that at a cell potential of -1.5 V, hydrogen (H_2, FE of 54.9%±1.4) and CO (FE of 40.1%±1.8) are the dominant products. However, our measurements indicate that by increasing the cell potential a system becomes more selective for CH_4 formation with the maximum FE of 82.7%±2 at a cell potential of -2.1 V. At this potential, W_2C NFs slightly produce other products such as C_2H_4, CH_3OH, C_2H_5OH, CO, and H_2 with FEs of 5.6%, 1.4%, 1.2%, 6.1%, and 1.4%, respectively. Figure 5b shows the maximum CH_4, C_2H_4, CH_3OH, and C_2H_5OH current densities of -421.28, -27.31, -5.95, and -5.19 mA/cm^2 at the cell potential of -2.3 V, respectively, confirming high selectivity of W_2C NFs towards CH_4 as the main product.

Next, we coupled the electrolyzer to a triple junction photovoltaic (TJ-PV) cell with a maximum efficiency of 34.3% to determine the CO_2RR performance and energy efficiency of W_2C NFs in a solar-driven device (Supplementary section S17). The *j*-V characteristic curve of the TJ-PV cell under one sun illumination (100 mW/cm^2) using a sun simulator light source is shown in Supplementary Fig. S46. The operating point is chosen to provide a photo current density of -394.3 mA/cm^2 at a potential of -2.1 V which has the maximum FE of CH_4 (82.7%±2) calculated in the flow electrolyzer (Supplementary Fig. S47).

Figure 5c shows the current density of the solar-driven electrolyzer for a 700-hour continuous process at a potential of -2.1 V. The results shown in Fig. 5c indicate a negligible decrease (approximately 2%) in the

photo-current density of W_2C NFs over the 700-hour experiment while the corresponding photo-potential fluctuates between -2.08 to -2.12 V, confirming the high stability of W_2C NFs for CO_2RR.

The measured sun to CO_2RR products (CO, CH_4, C_2H_4, CH_3OH, and C_2H_5OH) as well as total solar-to-fuel efficiency (SFE) of W_2C NFs over a 700-hour process are shown in Fig. 5d (Supplementary section S17). As shown in this figure, an average sun to CH_4 production efficiency of 17.3% with negligible variation (2%) is achieved during the 700-hour continuous process. Considering other products, W_2C NFs show a SFE of 20.7%.

We also calculated the energy efficiency of CO_2RR in our developed flow electrolyzer and compared it with state-of-the-art catalytic systems in the literature (Supplementary section S16)[29,30,37,57,72]. As shown in this figure (Supplementary Fig. S45), a maximum energy efficiency of 62.3% was obtained for our developed flow electrolyzer using W_2C catalyst that is about 67% and 73% more efficient than Cu_{oh} (37.4%)[50] and recently developed Cu-ClPH (36.1%)[72] catalytic systems, respectively.

In summary, we have synthesized four members of TMCs with a formula of M_2C, *i.e.*, W_2C, Mo_2C, Nb_2C, and V_2C NFs using the carburization method followed by the liquid exfoliation technique and tested their catalytic performance for eCO_2RR in KOH:CC (3M:2M) electrolyte. The electrocatalytic performance studies of TMCs shows these materials are mainly selective for CH_4 formation with W_2C NFs having the best CO_2RR activity compared to the studied catalysts. For instance, a CO_2RR current density of -548.89 mA/cm^2 and a maximum CH_4 current density of -421.63 mA/cm^2 at the potential of -1.05 V vs RHE were observed for W_2C NFs. Our electrochemical results also indicate that adding choline chloride to the electrolyte enhances the formation of CO_2RR products by suppressing the HER for all studied TMCs. Moreover, the NMR and $^{13}CO_2$ isotope experiments confirm that the choline chloride remains stable during the electrochemical experiments. Atomic and molecular scale characterizations such as XPS, XRD, and STEM indicate that all synthesized TMCs have similar lattice structure of 1T with a dominant plane of (101) and almost the same average crystallite size of 25.4 nm. Furthermore, the electronic property analyses of TMCs reveal superior electronic properties of W_2C NFs: low work function; small charge transfer resistance in the electrochemical double layer region; and heavily reduced tungsten atoms at the surface, which may lead to the observed outstanding activity. Computational results also indicate that the studied TMCs spontaneously chemisorb CO_2 and water as compared to Cu. However, among the TMCs studied, W_2C exhibits the optimal combination for CH_4 production, with favorable adsorption energies of water and CO_2 coupled with spontaneous dissociation, and less costly protonation of OH*, which is the limiting step, with a low limiting potential in the range of -0.483 V to -0.744 V vs RHE. Using W_2C NFs, we have demonstrated a solar-driven flow electrolyzer that can work up to 700 hours with a solar to CH_4 efficiency and a total SFE of 17.3 and 20.7%, respectively, under one sun illumination. The demonstrated solar-driven flow electrolyzer using a non-precious metal catalyst (W_2C NFs) in this study achieves a maximum efficiency of 62.3% making it a good candidate to approach the commercially

relevant electrocatalytic CO_2RR. This opens a new direction toward a low cost, sustainable large-scale production of fuels from CO_2 that can be used any time any place.

Methods

Synthesis of TMCs: TMCs were prepared by carburization process in a dual zone tubular furnace with a controlled flow of CH_4 and H_2 mixture (volumetric ratio CH_4:H_2 of 1:9) at a temperature of 973 K. The obtained bulk powders were then collected and ground to fine powders in a mortar and pestle. Next, a certain amount of TMC powders were processed in isopropyl alcohol using an ultrasonic liquid processor (Sonics VibraCell VCX-130) to obtain a solution of TMC nanoflakes (NFs). The resulting solution was further centrifuged at 1000 rpm for 30 min and the top two-third of the solutions were collected and stored as the TMCs in a vial for cathode electrode preparation. The detailed explanation is provided in Supplementary section S1.

Electrochemical setup: A two-compartment three-electrode electrochemical cell was used to perform the fundamental study for cathodic half-cell reaction using the synthesized W_2C, Mo_2C, Nb_2C, and V_2C NFs and compared them with Au and Cu NPs. In the three-electrode cell study, the working electrode was prepared by drop-casting the catalysts (mass loading of 0.1 mg) on a glassy carbon electrode with a geometric surface area of 1 cm^2. The catalyst loading on the electrode was precisely controlled to be 0.1 mg/cm^2 on the glassy carbon electrode. Platinum (Pt) gauze 52 mesh (Alfa Aesar) and Ag/AgCl (BASi) were used as counter and reference electrodes, respectively. The cathode and anode parts of the cell were separated through an anion exchange membrane (Sustainion X37-50 Grade RT, Dioxide Materials). All experiments were performed in CO_2 saturated KOH:CC (3M:2M) electrolyte with a pH of 14.5 ± 0.1. A two-compartment zero-gap solid polymer electrolyte flow electrolyzer was used to study the electrochemical performance where the working and counter electrodes are separated using an anion exchange membrane. Working electrodes (cathode) were prepared by brush-coating the solution of studied catalysts (W_2C NFs, Au NPs, and Cu NPs) on gas diffusion layer (GDL, Sigracet 39 BC, Fuel Cell Store) electrodes with a geometrical surface area of 5 cm^2. The counter electrode (anode) was prepared using a similar procedure where IrO_2 powder (Sigma Aldrich) was used as the catalyst solution. The actual loadings of 0.1 ± 0.01 mg/cm^2 were determined by weighing the dry GDLs before catalyst deposition and coated GDLs after being dried in a vacuum-oven overnight. As a separator in our experiments, we used an anion exchange membrane (Sustainion X37-50 Grade RT, Dioxide Materials) which was treated in 1 M KOH overnight at 75°C and then washed with deionized water prior to use. Anolyte flow of KOH:CC (3M:2M) with a flow rate of 20 ml/min was fed to the anode compartment using a peristaltic pump (Masterflex, Cole-Parmer). A mass flow controller (SmartTrak 50, Sierra, calibrated with CO_2 gas) connected to the CO_2 humidifier kit, was used to feed the cathode compartment with a flow rate of 50 ml/min.

PV cell characterization

A solar-powered flow cell was assembled by connecting the solid polymer electrolyte flow electrolyzer to a triple-junction photovoltaic (TJ-PV) solar cell. The TJ-PV cell was characterized at different sun illuminations using a custom-made sun simulator light source and an InGaAs photodiode (Thorlabs, FDG03-CAL) with a known responsivity calibration curve. Our results indicated a maximum efficiency of 34.32 % under one sun illumination used in our study.

Electrochemical characterization

Electrochemical experiments were performed using a Biologic Potentiostat SP-150. The chronoamperometry (CA) technique was used to study the performance of TMC NFs *i.e.*, W_2C, Mo_2C, Nb_2C, and V_2C NFs and compared them with that of Au and Cu NPs. The CA experiments were carried out in the range of -0.45 to -1.05 V vs RHE potentials. All experiments were performed under identical experimental conditions. The linear sweep voltammetry (LSV) technique was used to study the fundamentals of the cathodic half-cell reaction in the three-electrode cell setup. LSV curves were obtained by sweeping the potential between + 0.2 and − 1.05 V vs. reversible hydrogen electrode (RHE) with scan rate of 20 mV/s. The conversion of Ag/AgCl reference electrode potential to RHE scale was calculated using Nernst equation considering the pH of solution (pH = 14.5).

Product characterization

A gas chromatography system (GC, SRI, 8610C) equipped with a flame ionization detector (FID) and a thermal conductivity detector (TCD) was used to detect and quantify the electrochemical CO_2RR products. Ultra-high purity helium (He) and nitrogen (N_2) gases (UHP 99.99%, Airgas) were used as the carrier gas to identify any possible type of product. the signal response of the FID and TCD to each gaseous product (*e.g.*, H_2, CO, CH_4, C_2H_4) was calibrated by analyzing a series of standard gas mixtures with known compositions prior to the experiments. To study the products, 1 mL sample of the headspace of the cell was injected to the GC system using a lock-in syringe (Hamilton). Moreover, an *in-situ* differential electrochemical mass spectrometer (DEMS, Hiden Analytical, HPR-40) was used to validate the obtained information from the GC system by continuously detecting all possible products, even at trace amounts (partial pressure of 1×10^{-13} Torr), during the electrochemical CO_2RR (CA experiment), resulting in a more precise measurement. The signal responses of the DEMS instrument for different products (H_2, CO, CH_4, C_2H_4, CH_3OH, and C_2H_5OH) were calibrated by feeding standard samples into the mass spectrometer. An electron energy of 70 eV was used for ionization of all species, with an emission current of 500 µA. All mass-selected product cations were detected by a secondary electron multiplier with a detector voltage of 1200 V for maximizing the signal to noise ratio of the products.

X-ray diffraction (XRD)

The XRD technique was used to identify the phase purity and crystallinity of all studied catalysts (W_2C, Mo_2C, Nb_2C, V_2C NFs, Au NPs, and Cu NPs) using a Bruker D2 PHASER diffractometer in Bragg–Brentano geometry employing a Ni filtered Cu *K*α radiation (1.5405 Å). The X-ray diffraction (XRD) patterns were

obtained using a LynxEye linear position sensitive detector and a step width of 0.2 °2θ with a counting time of 1 s/step.

X-ray photoelectron spectroscopy (XPS)

A Thermo-Scientific ESCALAB 250Xi instrument equipped with an electron flood and scanning ion gun was used to identify the oxidation states of the W_2C NFs. All obtained spectra were analyzed using Thermo-Avantage software, considering the standard carbon peak at 284.8 eV and relative sensitivity factors.

Ultra-violet photoelectron spectroscopy (UPS)

Surface work function measurements were carried out using the UPS technique. All UPS data were acquired by a Thermo-Scientific ESCALAB 250Xi instrument using He I (21.2 eV) ultraviolet radiation and a pass energy of 8.95 eV.

Scanning transmission electron microscopy (STEM)

W_2C NFs were characterized at atomic scale using a spherical aberration corrected JEOL JEM-ARM 200CF STEM with a cold field emission gun operating at 200 kV. High-angle annular dark-field (HAADF) detector with 22 mrd inner-detector angle and bright field (BF) detector were utilized to obtain the atomic resolution images.

Theoretical study

We performed a comparative DFT analysis for the observed catalytic activity and reactivity of W_2C NFs with Au and other TMCs using SIESTA package, with Perdew–Burke–Ernzerhof functional with a double-zeta with polarization (DZP) localized basis set and the norm-conserving Troullier-Martins pseudopotentials. Calculations of density of states for bulk and slab geometries of Au and TMCs were performed using the Effective Screening Method (ESM)[73] for Brillouin zones of the unit cells sampled by Monkhorst-Pack k-point grids of size 9 x 9 x 9 and 1 x 9 x 9, respectively, together with a plane-wave cutoff of 300.0 Ry. The optimization of the atomic positions and cell parameters were carried out using a conjugate-gradient algorithm until a maximum atomic force tolerance of 0.04 eV/Å and a maximum stress component along each periodic direction of lower than 1 GPa were achieved. The Vienna ab initio Simulation Package (VASP, version 5.4.4) with PAW (projector augmented wave method) and Perdew–Burke–Ernzerhof exchange-correlation functionals were used to analyze the adsorption free energies of various molecular species on the (101) surface of M_2C (M = W, V, Mo, Nb). All the VASP calculations were performed for neutral non spin-polarized systems and dipolar electrostatic correction was used along the normal to the surface of the slab. Next, we used the tetrahedron method with Blöchl corrections and 1 x 3 x 3 Monkhorst-Pack grid k-point sampling for the calculations of total electronic energy (smearing σ = 0.1). The adsorption free energies were then used within the computational hydrogen electrode (CHE) model[64–66] to evaluate the lowest free energy pathways and the limiting reaction potentials.

Declarations

Acknowledgments

Mohammad Asadi's work was supported by Illinois Institute of Technology start-up funding, Wanger Institute for Sustainable Energy Research (WISER) Institute for Sustainable Energy Research (WISER) seed fund (262029 221E 2300), American Institute of Architects (AIA) Upjohn Development Research Grant (387523 240M 2301) and the Soft and Hybrid Nanotechnology Experimental (SHyNE) Resource (NSF ECCS-152205) funding at Northwestern University. This work was also supported by the Molecular Foundry and its compute cluster (vulcan), managed by the High-Performance Computing Services Group, at Lawrence Berkeley National Laboratory (LBNL), and by the National Energy Research Scientific Computing Center (NERSC). Resources are provided by the Office of Science of the U.S. Department of Energy under contract No. DE-AC02-05CH11231. Reza Shahbazian-Yassar efforts were supported by NSF (DMR-1809439). We acknowledge the EPIC facility (NU*ANCE* Center, Northwestern University), which has received support from the MRSEC program (NSF DMR-1121262) at the Materials Research Center; the Nanoscale Science and Engineering Center (NSF EEC–0647560) at the International Institute for Nanotechnology; and the State of Illinois, through the International Institute for Nanotechnology. The authors acknowledge Rao Tatavarti from Micro-Link Device, Inc. at Chicago for providing the triple junction PV cell. This work made use of instruments in the Electron Microscopy Service (Research Resources Center, UIC). The acquisition of the UIC JEOL JEM-ARM200CF was supported by an MRI-R2 grant from the National Science Foundation (Award No. DMR-0959470).

Author Contributions

M.A. and M.E. conceived the idea of the work. M.E. synthesized the nanostructured materials. M.E. and R.A. designed and fabricated the experimental devices. M.E., A.K., A.R.B., P.N.M.D., and J.P. performed electrocatalysis experiments and data analysis. D.P., A.B., A.S.M. and J.Q carried out DFT calculations and CHE model analysis. M.E., K.K., and C.U.S., did the XRD characterization and analysis. M.E. and A.K. did the XPS, UPS and NMR characterizations. B.S., M.T.S. and R.S.Y. performed the STEM characterization. M.A. supervised M.E., A.K., A.R.B., P.N.M.D. and J.P. efforts. All authors discussed the results and assisted with manuscript preparation.

Competing financial interests

M.A., M.E., A.K., and A.R.B. filed a patent application. The other authors declare no competing financial interests.

Data and materials availability

The data supporting and findings of the study are available in the paper and its supplementary materials.

References

1. Ross, M. B. *et al.* Designing materials for electrochemical carbon dioxide recycling. *Nat. Catal.* **2**, 648–658 (2019).
2. Lewis, N. S. Toward Cost-Effective Solar Energy Use. *Science* **315**, 798–801 (2007).
3. Chen, Y., Lewis, N. S. & Xiang, C. Operational Constraints and Strategies for Systems to Effect the Sustainable, Solar-driven Reduction of Atmospheric CO_2. *Energy Environ. Sci.* **8**, 3663–3674 (2015).
4. Esmaeili Rad, F., Abbasian, J. & Arastoopour, H. Numerical simulation of CO_2 adsorption in a fluidized bed using solid-supported amine sorbent. *Can. J. Chem. Eng.* (2020).
5. Shih, C. F., Zhang, T., Li, J. & Bai, C. Powering the Future with Liquid Sunshine. *Joule* **2**, 1925–1949 (2018).
6. Birdja, Y. Y. *et al.* Advances and Challenges in Understanding the Electrocatalytic Conversion of Carbon Dioxide to Fuels. *Nat. Energy* **4**, 732–745 (2019).
7. Rosen, B. A. *et al.* Ionic Liquid–Mediated Selective Conversion of CO_2 to CO at Low Overpotentials. *Science* **334**, 643–644 (2011).
8. Asadi, M. *et al.* Nanostructured transition metal dichalcogenide electrocatalysts for CO_2 reduction in ionic liquid. *Science* **353**, 467–470 (2016).
9. Rosen, B. a., Zhu, W., Kaul, G., Salehi-Khojin, a. & Masel, R. I. Water Enhancement of CO2 Conversion on Silver in 1-Ethyl-3-Methylimidazolium Tetrafluoroborate. *J. Electrochem. Soc.* **160**, H138–H141 (2012).
10. Abbasi, P. *et al.* Tailoring the Edge Structure of Molybdenum Disulfide toward Electrocatalytic Reduction of Carbon Dioxide. *ACS Nano* **11**, 453–460 (2017).
11. Asadi, M. *et al.* Robust carbon dioxide reduction on molybdenum disulphide edges. *Nat. Commun.* **5**, 4470 (2014).
12. Chan, K., Tsai, C., Hansen, H. A. & Nørskov, J. K. Molybdenum sulfides and selenides as possible electrocatalysts for CO_2 reduction. *ChemCatChem* **6**, 1899–1905 (2014).
13. Hong, X., Chan, K., Tsai, C. & Nørskov, J. K. How Doped MoS_2 Breaks Transition-Metal Scaling Relations for CO_2 Electrochemical Reduction. *ACS Catal.* **6**, 4428–4437 (2016).
14. Clark, E. L. *et al.* Influence of Atomic Surface Structure on the Activity of Ag for the Electrochemical Reduction of CO_2 to CO. *ACS Catal.* **9**, 4006–4014 (2019).
15. Rosen, J. *et al.* Mechanistic Insights into the Electrochemical Reduction of CO_2 to CO on Nanostructured Ag Surfaces. *ACS Catal.* **5**, 4293–4299 (2015).
16. Fang, Y. & Flake, J. C. Electrochemical Reduction of CO_2 at Functionalized Au Electrodes. *J. Am. Chem. Soc.* **139**, 3399–3405 (2017).
17. Zhao, Y., Wang, C., Liu, Y., MacFarlane, D. R. & Wallace, G. G. Engineering Surface Amine Modifiers of Ultrasmall Gold Nanoparticles Supported on Reduced Graphene Oxide for Improved Electrochemical CO_2 Reduction. *Adv. Energy Mater.* **8**, 1801400 (2018).

18. Lee, H. E. *et al.* Concave Rhombic Dodecahedral Au Nanocatalyst with Multiple High-Index Facets for CO_2 Reduction. *ACS Nano* **9**, 8384–8393 (2015).
19. Zhao, S., Jin, R. & Jin, R. Opportunities and Challenges in CO_2 Reduction by Gold- and Silver-Based Electrocatalysts: From Bulk Metals to Nanoparticles and Atomically Precise Nanoclusters. *ACS Energy Lett.* **3**, 452–462 (2018).
20. Zhang, Z. *et al.* Rational Design of Bi Nanoparticles for Efficient Electrochemical CO_2 Reduction: The Elucidation of Size and Surface Condition Effects. *ACS Catal.* **6**, 6255–6264 (2016).
21. Todoroki, N. *et al.* Surface Atomic Arrangement Dependence of Electrochemical CO_2 Reduction on Gold: Online Electrochemical Mass Spectrometric Study on Low-Index Au(hkl) Surfaces. *ACS Catal.* **9**, 1383–1388 (2019).
22. Back, S., Yeom, M. S. & Jung, Y. Active Sites of Au and Ag Nanoparticle Catalysts for CO_2 Electroreduction to CO. *ACS Catal.* **5**, 5089–5096 (2015).
23. Kim, K. S., Kim, W. J., Lim, H. K., Lee, E. K. & Kim, H. Tuned Chemical Bonding Ability of Au at Grain Boundaries for Enhanced Electrochemical CO_2 Reduction. *ACS Catal.* **6**, 4443–4448 (2016).
24. Tao, Z., Wu, Z., Yuan, X., Wu, Y. & Wang, H. Copper–Gold Interactions Enhancing Formate Production from Electrochemical CO_2 Reduction. *ACS Catal.* **9**, 10894–10898 (2019).
25. Morales-Guio, C. G. *et al.* Improved CO_2 reduction activity towards C2 + alcohols on a tandem gold on copper electrocatalyst. *Nat. Catal.* **1**, 764–771 (2018).
26. Liu, M. *et al.* Enhanced electrocatalytic CO_2 reduction via field-induced reagent concentration. *Nature* **537**, 382 (2016).
27. Asadi, M. *et al.* Highly Efficient Solar-Driven Carbon Dioxide Reduction on Molybdenum Disulfide Catalyst Using Choline Chloride-Based Electrolyte. *Adv. Energy Mater.* **0**, 1803536
28. Nitopi, S. *et al.* Progress and Perspectives of Electrochemical CO_2 Reduction on Copper in Aqueous Electrolyte. *Chem. Rev.* **119**, 7610–7672 (2019).
29. Dinh, C. T. *et al.* CO_2 electroreduction to ethylene via hydroxide-mediated copper catalysis at an abrupt interface. *Science* **360**, 783–787 (2018).
30. Li, F. *et al.* Molecular tuning of CO_2-to-ethylene conversion. *Nature* **577**, 509–513 (2020).
31. Wakerley, D. *et al.* Bio-inspired hydrophobicity promotes CO_2 reduction on a Cu surface. *Nat. Mater.* **18**, 1222–1227 (2019).
32. Jiang, K. *et al.* Metal ion cycling of Cu foil for selective C–C coupling in electrochemical CO_2 reduction. *Nat. Catal.* **1**, 111–119 (2018).
33. Zhang, X., Sun, X., Guo, S. X., Bond, A. M. & Zhang, J. Formation of lattice-dislocated bismuth nanowires on copper foam for enhanced electrocatalytic CO_2 reduction at low overpotential. *Energy Environ. Sci.* **12**, 1334–1340 (2019).
34. Iijima, G., Inomata, T., Yamaguchi, H., Ito, M. & Masuda, H. Role of a Hydroxide Layer on Cu Electrodes in Electrochemical CO_2 Reduction. *ACS Catal.* **9**, 6305–6319 (2019).

35. Liang, Z. *et al.* Copper-on-nitride enhances the stable electrosynthesis of multi-carbon products from CO_2. *Nat. Commun.* **9**, 3828 (2018).
36. Garza, A. J., Bell, A. T. & Head-Gordon, M. Mechanism of CO_2 Reduction at Copper Surfaces: Pathways to C_2 Products. *ACS Catal.* **8**, 1490–1499 (2018).
37. Ringe, S. *et al.* Understanding cation effects in electrochemical CO_2 reduction. *Energy Environ. Sci.* **12**, 3001–3014 (2019).
38. Li, C. W. & Kanan, M. W. CO_2 Reduction at Low Overpotential on Cu Electrodes Resulting from the Reduction of Thick Cu_2O Films. *J. Am. Chem. Soc.* **134**, 7231–7234 (2012).
39. Gogotsi, Y. & Anasori, B. The Rise of MXenes. *ACS Nano* **13**, 8491–8494 (2019).
40. Anasori, B. *et al.* Two-Dimensional, Ordered, Double Transition Metals Carbides (MXenes). *ACS Nano* **9**, 9507–9516 (2015).
41. Hantanasirisakul, K. & Gogotsi, Y. Electronic and Optical Properties of 2D Transition Metal Carbides and Nitrides (MXenes). *Adv. Mater.* **30**, 1804779 (2018).
42. Esmaeilirad, M., Kondori, A., Ruiz Belmonte, A. & Asadi, M. Electroreduction of Carbon Dioxide to Methane Enabled By Molybdenum Carbide Nanocatalyst. *ECS Meet. Abstr.* **MA2020-02**, 3234 (2020).
43. Lei, J., Kutana, A. & Yakobson, B. I. Predicting stable phase monolayer Mo_2C (MXene), a superconductor with chemically-tunable critical temperature. *J. Mater. Chem. C* **5**, 3438–3444 (2017).
44. Lewandowski, M., Szyma, A., Sayag, C. & Beaunier, P. Applied Catalysis B: Environmental Atomic level characterization and sulfur resistance of unsupported W_2C during dibenzothiophene hydrodesulfurization. Classical kinetic simulation of the reaction. *Applied Catalysis B: Environmental* **144**, 750–759 (2014).
45. Kondori, A. *et al.* Identifying Catalytic Active Sites of Trimolybdenum Phosphide (Mo_3P) for Electrochemical Hydrogen Evolution. *Adv. Energy Mater.* **9**, 1900516 (2019).
46. Esmaeilirad, M. *et al.* Oxygen Functionalized Copper Nanoparticles for Solar-Driven Conversion of Carbon Dioxide to Methane. *ACS Nano* **14**, 2099–2108 (2020).
47. Vasilyev, D. V & Dyson, P. J. The Role of Organic Promoters in the Electroreduction of Carbon Dioxide. *ACS Catal.* **11**, 1392–1405 (2021).
48. Zhang, T. *et al.* Highly dispersed, single-site copper catalysts for the electroreduction of CO_2 to methane. *J. Electroanal. Chem.* 113862 (2020).
49. Wu, J. *et al.* A metal-free electrocatalyst for carbon dioxide reduction to multi-carbon hydrocarbons and oxygenates. *Nat. Commun.* **7**, 13869 (2016).
50. De Gregorio, G. L. *et al.* Facet-Dependent Selectivity of Cu Catalysts in Electrochemical CO_2 Reduction at Commercially Viable Current Densities. *ACS Catal.* **10**, 4854–4862 (2020).
51. Chen, S. *et al.* Highly Selective Carbon Dioxide Electroreduction on Structure-Evolved Copper Perovskite Oxide toward Methane Production. *ACS Catal.* **10**, 4640–4646 (2020).

52. Wang, X. *et al.* Efficient Methane Electrosynthesis Enabled by Tuning Local CO2 Availability. *J. Am. Chem. Soc.* **142**, 3525–3531 (2020).
53. Weng, Z. *et al.* Active sites of copper-complex catalytic materials for electrochemical carbon dioxide reduction. *Nat. Commun.* **9**, 415 (2018).
54. Manthiram, K., Beberwyck, B. J. & Alivisatos, A. P. Enhanced Electrochemical Methanation of Carbon Dioxide with a Dispersible Nanoscale Copper Catalyst. *J. Am. Chem. Soc.* **136**, 13319–13325 (2014).
55. Jones, J. P., Prakash, G. K. S. & Olah, G. A. Electrochemical CO_2 Reduction: Recent Advances and Current Trends. *Isr. J. Chem.* **54**, 1451–1466 (2014).
56. Kuhl, K. P., Cave, E. R., Abram, D. N. & Jaramillo, T. F. New insights into the electrochemical reduction of carbon dioxide on metallic copper surfaces. *Energy Environ. Sci.* **5**, 7050–7059 (2012).
57. Hoang, T. T. H. *et al.* Nanoporous Copper–Silver Alloys by Additive-Controlled Electrodeposition for the Selective Electroreduction of CO_2 to Ethylene and Ethanol. *J. Am. Chem. Soc.* **140**, 5791–5797 (2018).
58. Kim, S. K., Zhang, Y. J., Bergstrom, H., Michalsky, R. & Peterson, A. Understanding the Low-Overpotential Production of CH_4 from CO_2 on Mo_2C Catalysts. *ACS Catal.* **6**, 2003–2013 (2016).
59. Holzwarth, U. & Gibson, N. The Scherrer equation versus the Debye-Scherrer equation. *Nat. Nanotechnol.* **6**, 534 (2011).
60. Patterson, A. L. The Scherrer Formula for X-Ray Particle Size Determination. *Phys. Rev.* **56**, 978–982 (1939).
61. Esmaeilirad, M., Zabihi, M., Shayegan, J. & Khorasheh, F. Oxidation of toluene in humid air by metal oxides supported on Γ-alumina. *J. Hazard. Mater.* **333**, 293–307 (2017).
62. Wang, Q. H., Kalantar-Zadeh, K., Kis, A., Coleman, J. N. & Strano, M. S. Electronics and optoelectronics of two-dimensional transition metal dichalcogenides. *Nat. Nanotechnol.* **7**, 699–712 (2012).
63. Bienen, F., Kopljar, D., Geiger, S., Wagner, N. & Friedrich, K. A. Investigation of CO_2 Electrolysis on Tin Foil by Electrochemical Impedance Spectroscopy. *ACS Sustain. Chem. Eng.* **8**, 5192–5199 (2020).
64. Nørskov, J. K. *et al.* Origin of the Overpotential for Oxygen Reduction at a Fuel-Cell Cathode. *J. Phys. Chem. B* **108**, 17886–17892 (2004).
65. Rossmeisl, J., Logadottir, A. & Nørskov, J. K. Electrolysis of water on (oxidized) metal surfaces. *Chem. Phys.* **319**, 178–184 (2005).
66. Peterson, A. A., Abild-Pedersen, F., Studt, F., Rossmeisl, J. & Nørskov, J. K. How copper catalyzes the electroreduction of carbon dioxide into hydrocarbon fuels. *Energy Environ. Sci.* **3**, 1311–1315 (2010).
67. Li, N. *et al.* Understanding of Electrochemical Mechanisms for CO_2 Capture and Conversion into Hydrocarbon Fuels in Transition-Metal Carbides (MXenes). *ACS Nano* **11**, 10825–10833 (2017).
68. Garza, A. J., Bell, A. T. & Head-Gordon, M. Is Subsurface Oxygen Necessary for the Electrochemical Reduction of CO_2 on Copper? *J. Phys. Chem. Lett.* **9**, 601–606 (2018).

69. Favaro, M. *et al.* Subsurface oxide plays a critical role in CO_2 activation by Cu(111) surfaces to form chemisorbed CO_2, the first step in reduction of CO_2. *Proc. Natl. Acad. Sci.* **114**, 6706–6711 (2017).
70. Lim, D. H. *et al.* Carbon dioxide conversion into hydrocarbon fuels on defective graphene-supported Cu nanoparticles from first principles. *Nanoscale* **6**, 5087–5092 (2014).
71. Kondori, A. *et al.* Kinetically Stable Oxide Overlayers on Mo_3P Nanoparticles Enabling Lithium–Air Batteries with Low Overpotentials and Long Cycle Life. *Adv. Mater.* **32**, 2004028 (2020).
72. García de Arquer, F. P. *et al.* CO_2 electrolysis to multicarabon products at activities greater than 1 A cm^{-2}. *Science* **367**, 661 LP – 666 (2020).
73. Otani, M. & Sugino, O. First-principles calculations of charged surfaces and interfaces: A plane-wave nonrepeated slab approach. *Phys. Rev. B* **73**, 115407 (2006).

Figures

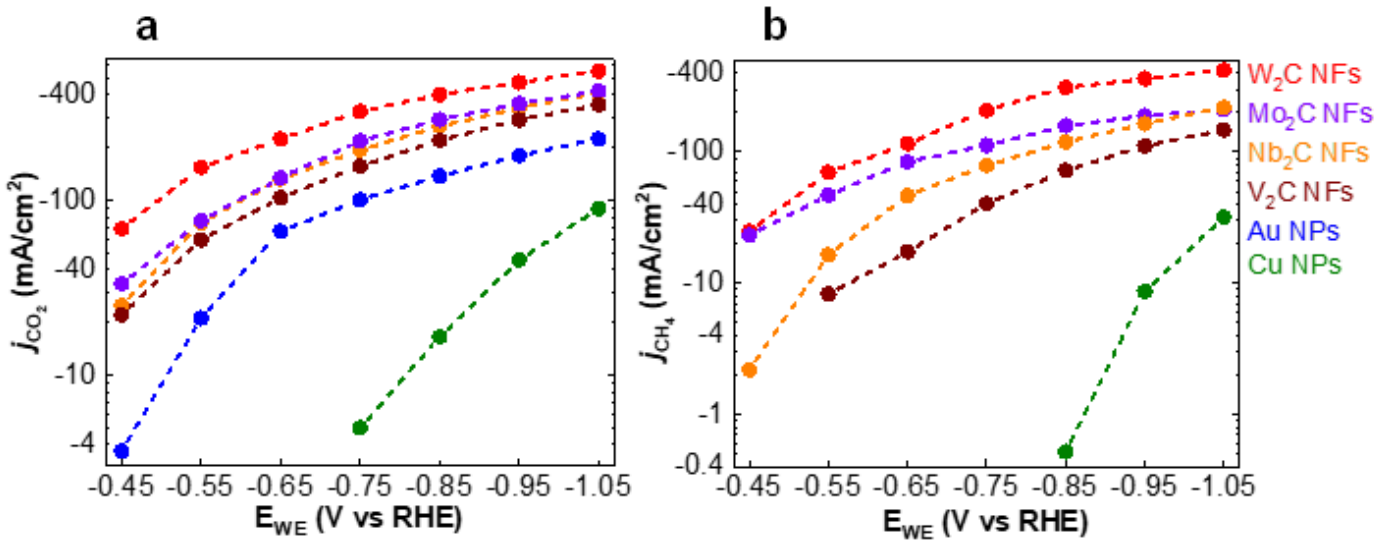

Figure 1

Electrocatalytic performance of TMCs i.e., W2C, Mo2C, Nb2C, V2C NFs in the two-compartment three-electrode electrochemical cell using CO2 saturated KOH:CC (3M:2M) electrolyte. (a) CO2 reduction reaction current densities of TMCs compared to Au and Cu NPs at different potentials under identical experimental condition. (b) CH4 formation current densities of TMCs compared to Cu NPs at different potentials under identical experimental condition.

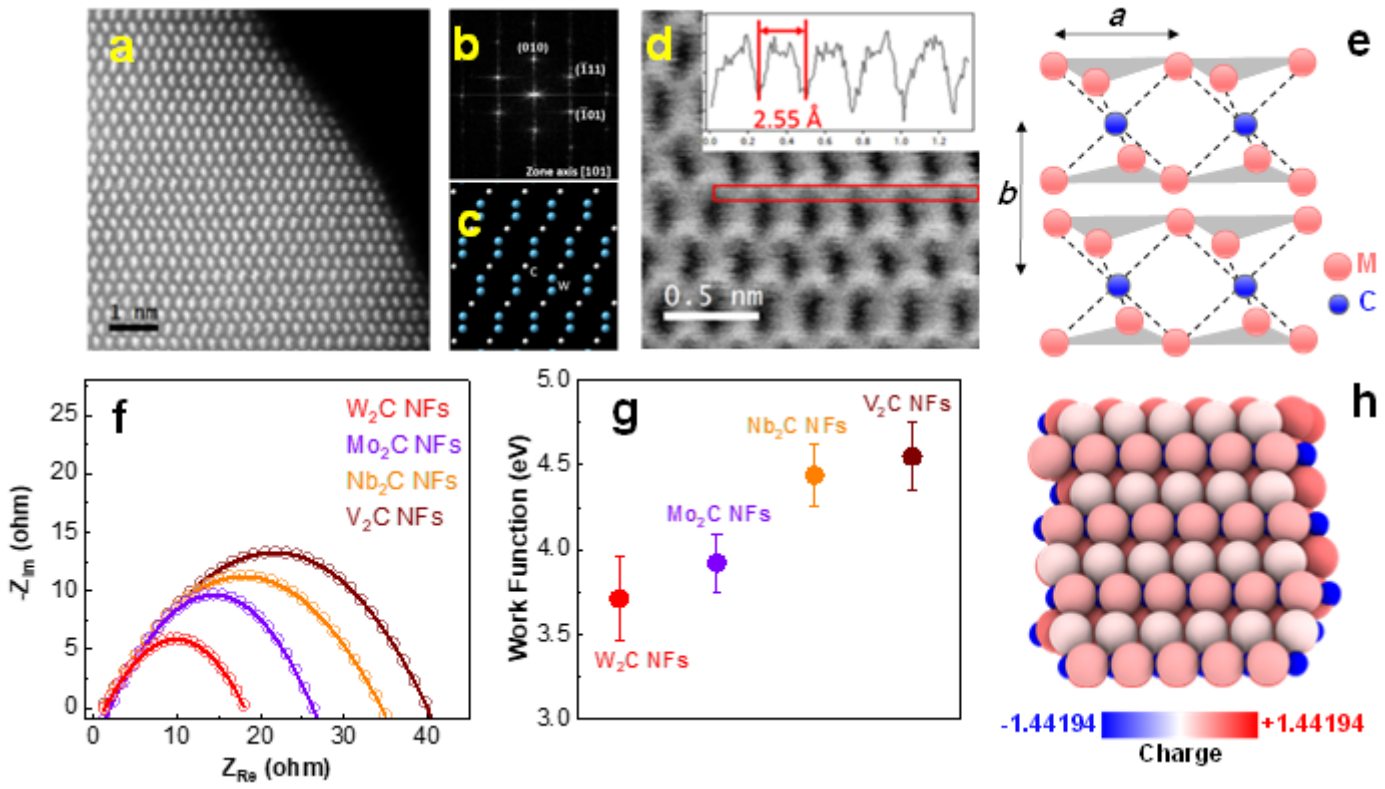

Figure 2

Structural and electrochemical characterization of TMC catalysts. (a) High-angle annular dark-field (HAADF) of W2C NFs in <101> zone axis. (b) FFT corresponding to the HAADF image of W2C NFs showing the diffraction spots from <101> zone axis. (c) Atomic model of W2C NFs in <101> zone axis. W atoms are shown as blue and carbon atoms as white spheres. (d) Bright field (BF) of W2C NFs in <101> zone axis. It shows the carbon atomic columns in red box. The inset is intensity profile across red box region showing distance between two carbon atoms is 2.55 Å. (e) Schematic of 1T structure TMCs showing tetragonal symmetry, one layer per repeat unit with octahedral coordination. The transition metal atoms (i.e., W, Mo, Nb, V) are red and the carbon atoms are blue. The lattice constant a is in the range of 3.07 to 3.15 Å for synthesized TMCs. The stacking index b indicates the interlayer spacing which is in the range of 4.53 to 5 Å for studied TMCs. (f) Electrochemical impedance spectroscopy (EIS) for studied catalysts at a potential of -310 mV vs RHE in the two-compartment three-electrode electrochemical cell using KOH:CC (3M:2M) electrolyte. (g) Work function measurements for synthesized TMCs using ultraviolet photoelectron spectroscopy (UPS) method. (h) Bader charges of W2C NFs indicate that surface W-atoms are contributing significantly to the catalytic activity of the W2C (101) surface.

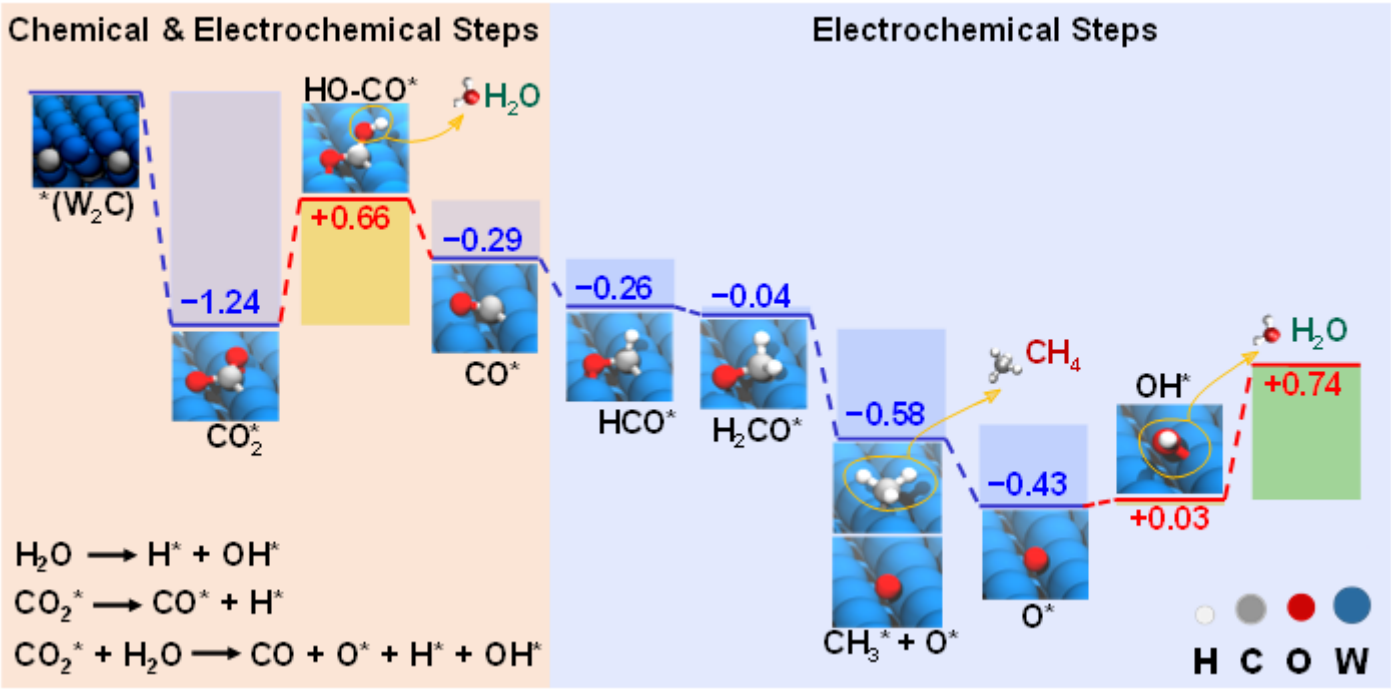

Figure 3

Minimum energy path for the electrochemical CO2 conversion into CH4 on the surface of W2C NFs. Only electrochemical steps are shown. The parts of the reaction where chemical and electrochemical steps are essential are highlighted by colors. The favorable reactions of key chemical steps are provided (for free energies of these reactions, see Table S9). The intermediates are indicated. Gibbs free energies for reaction at zero potential vs. RHE are given in eV.

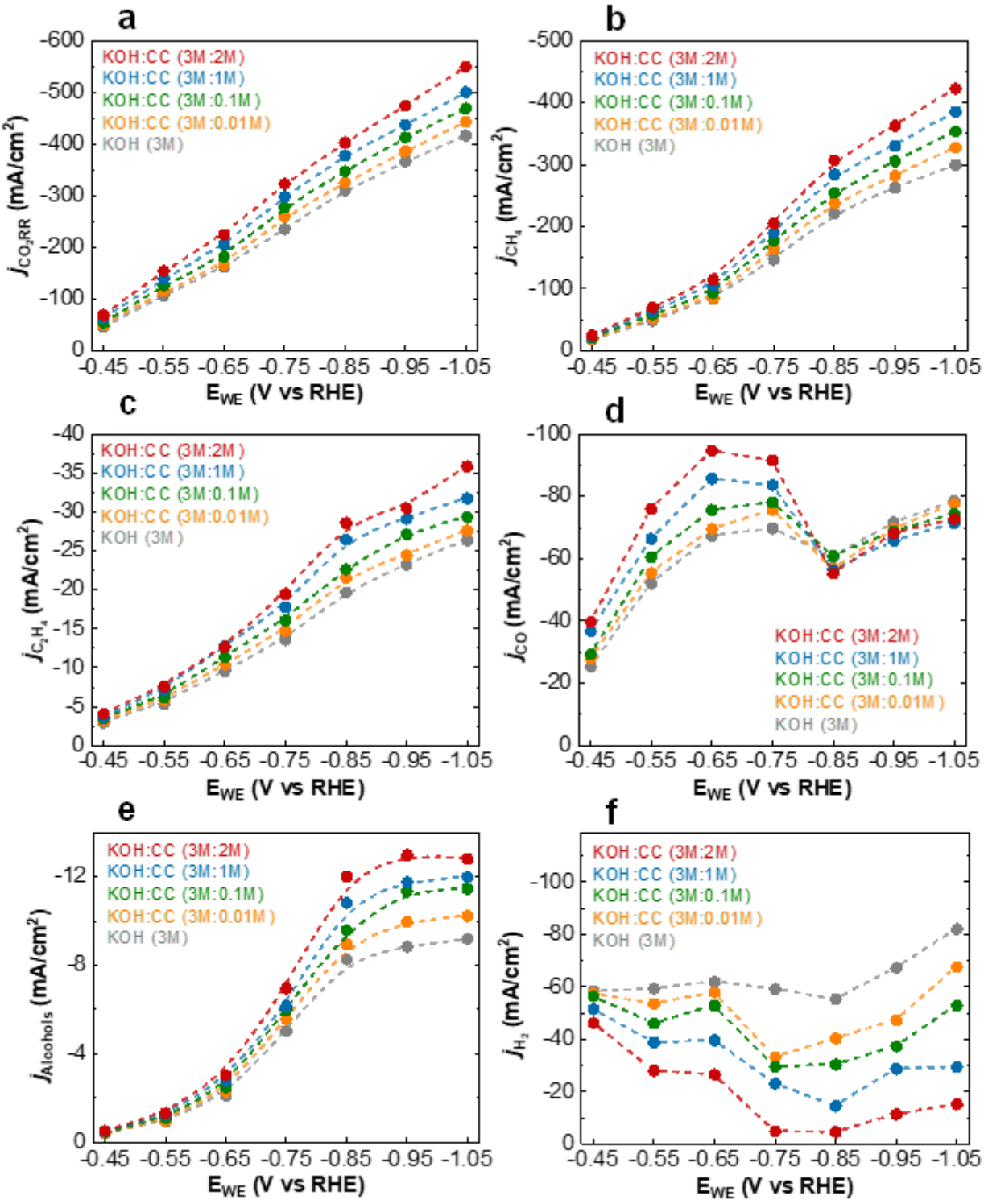

Figure 4

Effect of choline chloride in the electrochemical performance of W2C NFs for CO2RR. The values are measured using 3 M KOH and mixed 3 M KOH with different concentrations (0.1, 0.01, 1 and 2 M) of choline chloride (CC) electrolytes. Partial current density measurements for (a) CO2RR, (b) CH4 (c) C2H4, (d) CO, (e) Alcohols (CH3OH and C2H5OH) and (f) H2 as a function of potential.

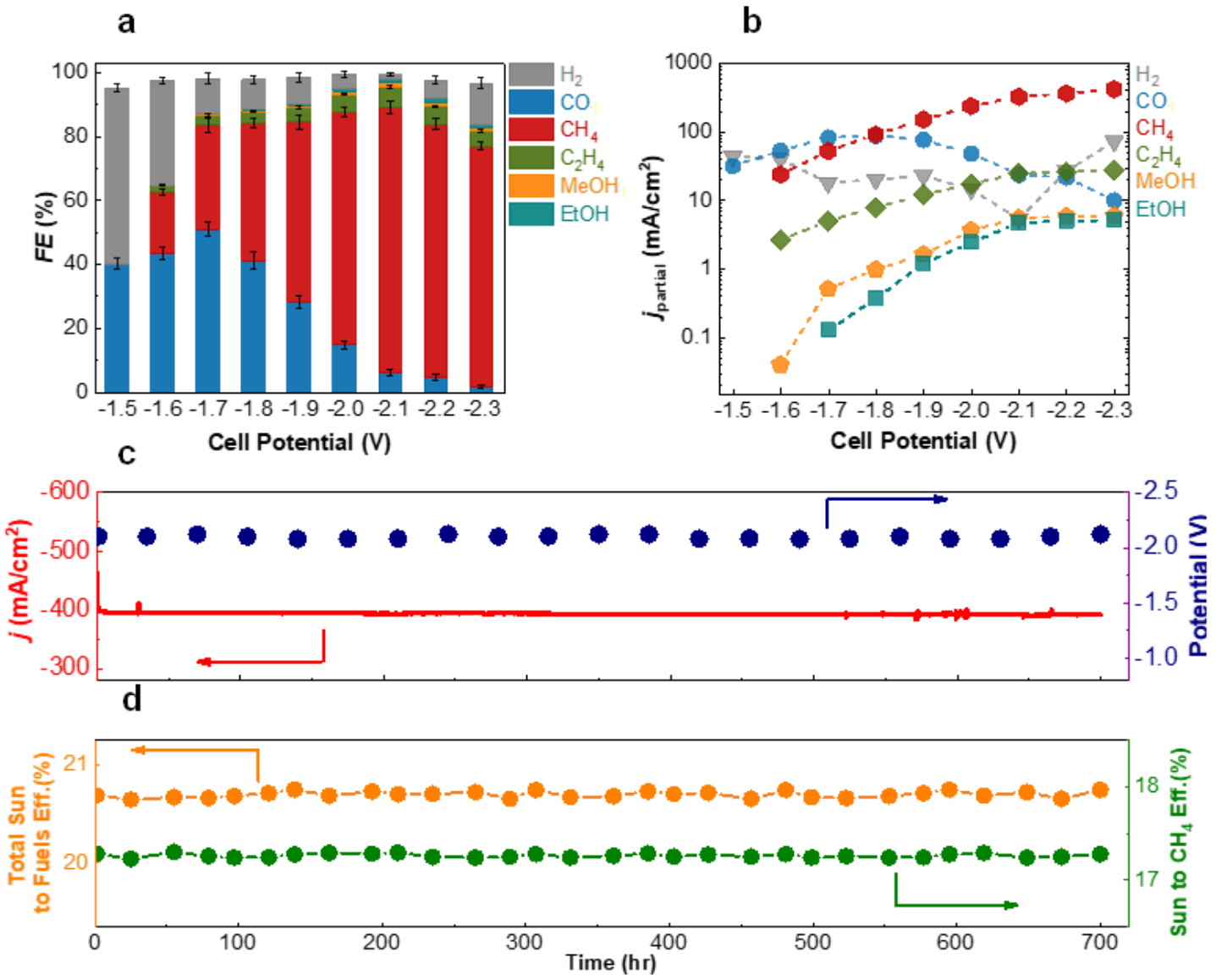

Figure 5

Electrocatalytic performance and stability of W2C NFs in the solid polymer electrolyte flow electrolyzer. (a) Faradaic efficiency (FE) measurements of H2, CO, CH4, C2H4, methanol (MeOH) and ethanol (EtOH) for W2C NFs at different cell potentials. The error bars represent standard deviations of four independent experiments. (b) Partial current density for each product as a function of cell potential. The values are obtained considering total current density and faradaic efficiencies of products at the entire range of cell potential. (c) Measured total current densities and cell potentials of the solar-driven solid polymer electrolyte flow electrolyzer under one sun illumination provided by the TJ-PV cell over the time. (d) Total sun to fuels efficiency and sun to CH4 production efficiency in the solar-driven solid polymer electrolyte flow electrolyzer over the time.

Supplementary Files

This is a list of supplementary files associated with this preprint. Click to download.

- TMCsSupplementaryMaterialsFinal.docx